Journal of Innovative Technology, Vol. 4, No. 2, pp. 65-73, September 2022
http://doi.org/10.29424/JIT.202209_4(2).0007

Simulation of Volume Energy Density Effect on Roughness in Selective Laser Melting

Shyang-Jye Chang [1], Han-Yun Tsai [2]

ABSTRACT

Selective Laser Melting (SLM) is a manufacturing method in which the metal powder is used as a material, and a layer of powder is deposited with a roller and then melted with a high-energy laser beam to build each layer of a part. The product made by SLM has a density close to 100% of material. However, its performance in surface quality is not satisfactory. In this study, the finite element simulation software was used to analyze the manufacturing process parameters and temperature distribution in the single melting trajectory and multiple melting trajectories SLM process. The simulation results were compared with the experimental results to verify the influence of temperature distribution on surface roughness. In the single track simulation, the simulation results meet with the experimental results. At the same laser power, the faster the speed, the lower the energy density, and as the volumetric energy density decreases, the track width shrinks. In multiple track simulation, the temperature increases as the number of scan track increases until the maximum temperature, and the thermal accumulation effect is clearly observed in the temperature profile. It was found in the simulation results that when the maximum temperature is near the melting point of the metal, the surface quality of the specimen will be better. Therefore, controlling the temperature, that is, controlling the scanning speed and laser power, is very important when selecting a SLM process parameter.

Keywords: selective laser melting; volume energy density; finite element analysis

1. INTRODUCTION

Additive manufacturing (AM) is popular and widely used in the industries over the recent years. Additive manufacturing systems are able to manufacture three-dimensional components and products directly from raw materials and 3D design data. The layer-by-layer operating process of these systems does not require the use of tools, molds, or dies [1]. Freedom of design, mass customization, waste minimization, and the ability to manufacture complex structures, as well as fast prototyping, are the main benefits of additive manufacturing or 3D printing [2]. According to the marketing report, with the global additive manufacturing market in 2018, including hardware, software, materials and services, stands at $9.3 billion in generated revenues after growing 18% [3]. Selective Laser Melting (SLM) is a particular rapid prototyping, 3D printing, or Additive Manufacturing technique designed to use high power-density laser to melt and fuse metallic powders. A component is built by selectively melting and fusing powders within and between layers. The SLM technique is also commonly known as direct selective laser sintering, laser fusing, and direct metal laser sintering, and this technique has been proven to produce near net-shape parts up to 99.9% relative density. This enables the process to build near full density functional parts and has viable economic benefits. Recent developments of fiber optics and high-power laser have also enabled SLM to process different metallic materials, such as copper, Aluminum, and tungsten. Similarly, this has also opened up research opportunities in SLM of ceramic and composite materials [4]. Although the SLM process offers a great advantage in manufacturing complex parts at a high material utilization rate, it is affected by many factors, such as laser energy input and scan speed, scan strategy, powder material, powder size and morphology. The common defects are classified in three types: porosities, incomplete fusion holes, and cracks [5].

Thermal analysis of laser processes can be used to predict thermal stresses and microstructures during processing in a completed part. With the highly advancement of computer science, thermal analysis becomes more and more diversification, there are several ways to simulate physics phenomenon, such as FEM (Finite Element Method) and DEM (Discrete Element Method). Many researchers had studied in SLM process, such as the residual stress, thermal effect, particle size distribution, chamber temperature effect. Thermal analysis is the basis for feedback tuning of laser processing parameters in manufacturing. In many studies, experimental methods were commonly used to detect and validate thermal behavior during processing. In recent years, some temperature measuring systems have been implemented to validate the simulation results.

Laser power, scanning speed, powder layer thickness, particle size distribution are the major process parameters in SLM process. Some researchers have shown the optimization to improve the as-built surface quality.

Yadroitsev [8] analyzed the relation between processing parameters and surface roughness. With the excess scanning speed, pores became large and reduced surface quality. Moreover, smaller layer thickness (40μm -50μm) showed better performance on surface roughness in each group of experimental conditions. The

Manuscript received August 25, 2022; revised September 14, 2022; accepted September 20, 2022.

[1] Associate Professor (corresponding author), Department of Mechanical Engineering, National Yunlin University of Science and Technology, Taiwan. (email: changjye@yuntech.edu.tw)

[2] Master Student, Department of Mechanical Engineering, National Yunlin University of Science and Technology, Taiwan.

hatch distance should be set up depending on the track width, which is relevant to surface roughness. Cherry [9] also revealed the low porosity of specimen is rated to better performance in both surface roughness and hardness. Surface balling is appeared to deteriorate surface quality under unfavourable energy densities. Spierings [10] confirmed that the coarser particle size distribution generates poor roughness. The minimal surface roughness of the specimen is appeared in the range of 50-90 J/mm3 under condition of 30μm layer thickness. However, the surface roughness is prone to be similar in the thicker powder layer(45μm). Mumtaz [11] surveyed processing parameters that affect top and side roughness. Unfortunately, it cannot acquire the smoothest surface roughness simultaneously. In the thermal physics of powder, Rombouts [12] revised that there's no clear correlation of the extinction coefficient with the powder material and particle size, and morphology is revealed, which is in line with the assumption of geometrical optics. Linear energy density is used by Wei [13] and Hong [14] to interpret experimental results of single trajectory. Ciurana [15] and Sabina [16] applied volumetric energy density to characterize stable single track, and layer thickness is regarded as the parameter in the formula. Wang [17] use another volumetric energy density formula to obtain single trajectory's characteristics. Hussein [18] used Gaussian distribution as the laser energy density to simulate the single layer SLM simulation research. Li [19] investigate the effects of laser power and scan speed on the SLM thermal behavior by using 3D FEM compared with the SLM experiment. Loh [20] revised that the melt penetration and width increased with increasing laser power and reduced scan speed. Increasing the laser power increases the total volume of powder molten and volume of molten powder evaporated. Alkahari [21] found out that air gap between metal powders particles contributed to low thermal conductivity of metal powder. Antony [22] used a finite element-based model of heat transfer to determinate the temperature distribution in the single powder layer. Foroozmehr [23] considers powder-to-solid transition together with an effective method to achieve volume shrinkage and material removal on FE model. Yin [24] found that the temperature increases with the laser power and decreases with the scan speed monotonously. The complex relationship can be found between the temperature and laser spot diameter during the laser single track. Dong [25] first use a Gaussian relationship to describe the laser intensity distribution across the beam diameter in selective laser sintering simulation. Trapp [26] studied the relations of absorptivity of metallic powders by laser fusion. Rombouts [27] revealed that Oxygen in the atmosphere of the SLM chamber increases the melt volume formed during SLM due to exothermic oxidation of Fe. Sih [28] revised a view factor for the prediction of the thermal conductivity of powder beds at high temperature that includes a radiation contribution to the conductivity.

Table 1 shows the studies on processing parameters and surface roughness in SLM process. In this study, the finite element analysis software simulating manufacturing process parameters were used to observe the temperature distribution single melting trajectory and multiple melting trajectories. The experimental parameters were compared with the experimental data to verify the influence of temperature distribution on surface roughness. In the FEM model, the laser heating energy is modeled as Gaussian distribution, and the influence of the particle size distribution and the laser wavelength is ignored to reduce the computer resource consumption. Through the heat transfer, two-phase flow phase field module in FEM software, the transition of the transition zone of the two-phase flow is simulated to analyze the change of the powder layer after melting.

Table 1 Studies on processing parameters and surface roughness in SLM process.

Year	Author	Method/Finding
2011	Yadroitsev [8]	Smaller layer thickness showed a better performance on surface roughness.
2015	Cherry [9]	Worse surface roughness appears under unfavorable energy density.
2011	Spierings [10]	Thicker powder layer has the better surface roughness. Particle size distribution is indeed a parameter need to be considered.
2005	Rombouts [12]	There's no clear correlation of the extinction coefficient with the powder material and particle size.
2015	Loh [20]	The melt penetration and width increased with increasing laser power and reduced scan speed. Increasing the laser power increases the total volume of powder molten and volume of molten powder evaporated.
2013	Husseiin [18]	Using Gaussian distribution as the laser energy to simulate the single layer of SLM simulation research.
2014	Li [19]	The moving laser heat source acting on the powder bed was modeled as the Gaussian distribution of heat flux and was input directly on the surface of the powder layer.
2014	Antony [22]	Using a finite element-based model to determine the temperature distribution in the single powder layer.
2016	Foroozmehr [23]	Considers powder-to-solid transition together with an effective method to achieve volume shrinkage and material removal on FE model.
2017	Trapp [26]	The power dependency of the absorptivity for the powder coated case at high intensities is qualitatively similar to the flat plate.

2. MATERIALS AND METHODS

2.1 Simulation Method

Powder based selective laser melting involves using a direct laser beam to melt a thin powder layer in the nitrogen chamber that condenses and solidifies onto a substrate. The process includes absorption of laser radiation on the metal surface, conductive and convective heat transfer in the metal and the ambient atmosphere as well as melting, solidification, evaporation and condensation. The physical phenomena in SLM process is essentially a heat transfer procedure. The path of the beam can be defined in terms of the beam center on the surface of the powder layer as a function of time. The thermo-fluid dynamical for SLM is simulated by using the fluid dynamics and the heat transfer module of the finite element simulation software package Comsol Multiphysics.

The relationship between volumetric energy density and single trajectory must be observed first to obtain the relationship between surface and volumetric energy density, and then the appropriate combination of volumetric energy density parameters is obtained. A single-layer laser melting simulation is established

by appropriate parameters. In order to verify and analyze the relationship between volumetric energy density and surface roughness, three sets of parameters from the experimental data are used to explore the relationship between temperature distribution and surface roughness.

2.2 Material Properties

SUS 316L stainless steel is the material used in the model. The detailed properties [26-28] is in Table 2.

Table 2 SUS 316L material properties.

	Melting point 1700 K	Vaporizing point 3000 K
Density [kg/m^3]	7430	6740
Dynamic viscosity of fluid [pa·s]	4.37×10^{-3}	2.7×10^{-3}
Thermal conductivity [W/(m·K)]	35.95	22.25
Heat capacitance [J/(kg·K)]	965	600
Surface tension [N/m]	1.70	1.72

2.3 Model Equations For Additive Manufacturing Process

2.3.1 Energy density

This research uses volumetric energy density [15] to interpret experimental results of single trajectory.

$$\text{VED}=\frac{P}{v\sigma t}\,[J/mm^3] \tag{1}$$

where P is the laser power, v is the scanning speed, σ laser beam diameter and t is the powder layer thickness.

2.3.2 Heat transfer

The heat transfer model for the process is modelled as a transient heat conduction problem with a moving heat source and can be written as follows.

$$\mathrm{Q}=\rho C_p\frac{\partial T}{\partial t}+\rho C_p\boldsymbol{u}\cdot\nabla T+\nabla\cdot\boldsymbol{q} \tag{2}$$

$$\mathbf{q}=-\mathrm{k}\nabla\mathrm{T} \tag{3}$$

where ρ is the material density (kg/m3), Cp is the specific heat capacity (J/kg·K), T is the temperature (K), t is the interaction of time, u is the speed of the fluid, q is the heat flux by conduction, k is the thermal conductivity of the material.

2.3.3 Laser heat input

The heating due to laser is treated as a body heat source, the body heat load within the metal powder plate is given by the following expression.

$$\mathrm{Q(x,y,z)}=Q_0\cdot(1-R_c)\cdot\frac{A_c}{\pi\sigma_x\sigma_y}\cdot e^{-\left[\frac{(x-x_0)^2}{2\sigma_x^2}+\frac{(y-y_0)^2}{2\sigma_y^2}\right]}\cdot e^{-A_cz} \tag{4}$$

where Q0 is the total power input, Rc is the reflection coefficient, Ac is the absorption coefficient, σx, σy are the standard deviation parameters, $e^{-\left[\frac{(x-x_0)^2}{2\sigma_x^2}+\frac{(y-y_0)^2}{2\sigma_y^2}\right]}$ is the 2D Gaussian distribution in x-y plane, e-AcZ is the exponential decay due to absorption.

2.3.4 Laminal flow in SLM simulation

The fluid flow in SLM process is regarded as laminal flow. The single-phase flow interfaces are based on the Navier-Stokes equations, which in general form as follows, equation (5) is the continuity equation and represents conservation of mass, equation (6) is a vector equation which represents conservation of momentum, equation (7) describes the conservation of energy, formulated in terms of the temperature [29].

$$\frac{\partial\rho}{\partial t}+\nabla\cdot(\rho\boldsymbol{u})=0 \tag{5}$$

$$\rho\frac{\partial\boldsymbol{u}}{\partial t}+\rho(\boldsymbol{u}\cdot\nabla)\boldsymbol{u}=\nabla\cdot[-p\boldsymbol{I}+\tau]+\boldsymbol{F} \tag{6}$$

$$\rho C_p\left(\frac{\partial T}{\partial t}+(u\cdot\nabla)T\right)=-(\nabla\cdot q)+\tau:S-\frac{T}{\rho}\frac{\partial\rho}{\partial T}\Big|_p\left(\frac{\partial p}{\partial t}+(u\cdot\nabla)p\right)+\mathrm{Q} \tag{7}$$

where ρ is the density (kg/m3), u is the velocity vector (m/s), p is pressure (Pa), τ is the viscous stress tensor (Pa), F is the volume force vector (N/m3), Cp is the specific heat capacity at constant pressure (J/(kg·K)), T is the absolute temperature (K), q is the heat flux vector (W/m2), Q contains the heat sources (W/m3), S is the strain-rate tensor:

$$\boldsymbol{S}=\frac{1}{2}(\nabla\mathbf{u}+(\nabla\mathbf{u})^T) \tag{8}$$

and the operation ":" denotes a contraction between tensors defined by

$$\mathbf{a}:\mathbf{b}=\sum_n\sum_m a_{nm}b_{nm} \tag{9}$$

The dynamic viscosity, μ (Pa·s), for a Newtonian fluid is allowed to depend on the thermo-dynamic state but not on the velocity field.

$$\tau=2\mu\mathbf{S}-\frac{2}{3}\mu(\nabla\cdot\mathbf{u})\mathbf{I} \tag{10}$$

2.3.5 Incompressible flow with gravity

For incompressible flow the fluid density is assumed to be constant, and the gravity is added into the equation.

$$\rho\frac{\partial\boldsymbol{u}}{\partial t}+\rho(\boldsymbol{u}\cdot\nabla)\boldsymbol{u}=\nabla\cdot[-\rho\boldsymbol{I}+\boldsymbol{K}]+\boldsymbol{F}+\rho\boldsymbol{g} \tag{11}$$

$$\rho\nabla\cdot(\boldsymbol{u})=0 \tag{12}$$

$$\boldsymbol{K}=\mu(\nabla\boldsymbol{u}+(\nabla\boldsymbol{u})^{\mathrm{T}}) \tag{13}$$

2.2.6 Two phase flow field

Phase field interfaces use the incompressible formulation of the Navier-Stokes equations [29]:

$$\rho\frac{\partial u}{\partial t}+\rho(u\cdot\nabla)=\nabla\cdot[-pI+\mu(\nabla u+\nabla u^{T})]+F_g+F_{st}+F_{ext}+F \quad (14)$$

$$\nabla\cdot u=0 \quad (15)$$

where Fg is the gravity force which is equal to ρ ·g, where g is the gravity vector, Fext is the volume force which is equal to $(\frac{\partial f}{\partial\phi})\nabla\phi$, Fst is the surface tension force for the phase field method which is implemented as a body force and is equal to $(G-\frac{\partial f}{\partial\phi})\nabla\phi$, G is the chemical potential (J/m3).

Phase field method is used to track the interface, the following equations is added necessary:

$$\frac{\partial\phi}{\partial t}+u\cdot\nabla\phi=\nabla\cdot\frac{\gamma\lambda}{\varepsilon^2}\nabla\psi \quad (16)$$

$$\psi=-\nabla\cdot\varepsilon^2\nabla\phi+\left(\phi^2-1\right)\phi+\left(\frac{\varepsilon^2}{\lambda}\right)\frac{\partial f_{ext}}{\partial\phi} \quad (17)$$

where the quantity λ (N) is the mixing energy density and ε (m) is a capillary width that scales with the thickness of the interface. These two parameters are related to the surface tension coefficient, σ (N/m), through the equation

$$\sigma=\frac{2\sqrt{2}}{3}\frac{\lambda}{\varepsilon} \quad (18)$$

and γ is the mobility parameter which is related to ε through $\gamma=\chi\varepsilon^2$ where χ is the mobility tuning parameter (set to 1 by default). The volume fraction of Fluid 2 is computed as

$$V_f=\min\left(\max\left(\left[\frac{1+\phi}{2}\right],0\right),1\right) \quad (19)$$

where the min and max operators are used so that the volume fraction has a lower limit of 0 and an upper limit of 1. The density is then defined as

$$\rho=\rho_1+(\rho_2-\rho_1)V_f \quad (20)$$

and the dynamic viscosity according to

$$\mu=\mu_1+(\mu_2-\mu_1)V_f \quad (21)$$

where ρ1 and ρ2 are the densities and μ1 and μ2 are the dynamic viscosities of Fluid 1 and Fluid 2, respectively.

The mean curvature (1/m) can be computed by entering the following expression:

$$\kappa=2(1+\phi)(1-\phi)\frac{G}{\sigma} \quad (22)$$

where G is the chemical potential defined as:

$$G=\lambda\left(-\nabla^2\phi+\frac{\phi(\phi^2-1)}{\varepsilon^2}\right)+\frac{\partial f}{\partial\phi} \quad (23)$$

3. RESULTS

3.1 Analysis and Validation of Single Track Simulation

3.1.1 Temperature distribution varies with time

In the simulation model, powder layer is regarded as a bulk. There are three parts in this model, the substrate, the powder layer and the gas (shown as Figure.1 (a)). The size of the base plate is 660 um wide, 360 um long and 60 um high, the size of the powder layer is 660 um wide, 360 um long and 40 um high, the size of the nitrogen layer is 660 um wide, 360 um long and 100 um high.

Temperature distribution plays an important role in selective laser melting process, Figure 1 shows the temperature distribution at a different time under the scanning speed of 100 mm/s and laser power of 100W with the laser beam spot 60 μm. The maximum temperature locates at the center of the laser beam.

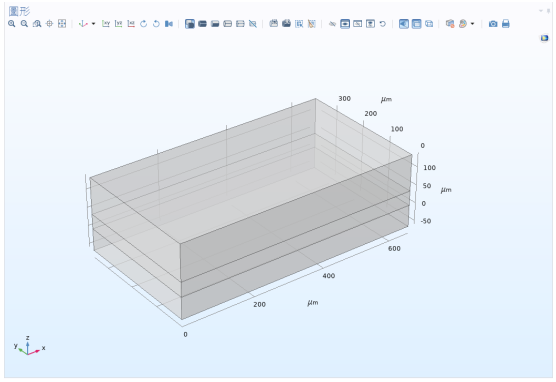

(a) scheme of simulation model

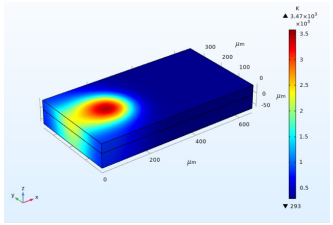

(b) t=0.00165

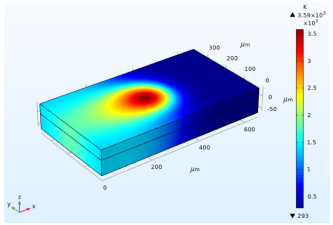

(c) t=0.0033

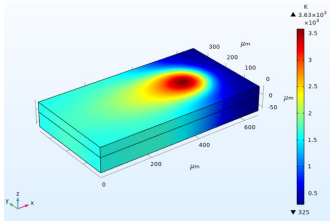

(d) t=0.00495

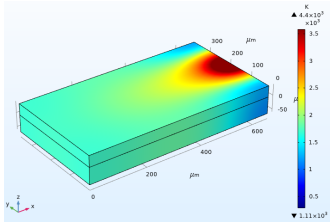

(e) t=0.0066

Fig. 1 Temperature distribution at t=0.00165, t=0.0033, t=0.00495, t=0.0066

3.1.2 Effect of scanning speed with temperature on manufacturing parts

For heat transfer analysis in various scanning speed, it is obviously that in the same laser power, the higher the scanning speed, the lower the temperature, as shown in Figure 2 and Figure 3. On the other hand, the temperature has the positive ratio with the VED magnitude, the higher the VED, the lower the temperature.

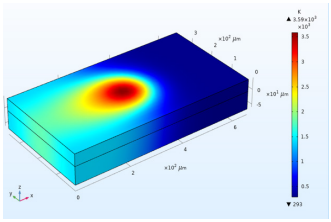

(a) Laser power 100 W, Scanning speed 100 mm/s

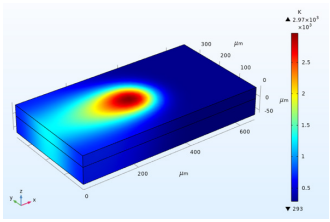

(b) Laser power 100 W, Scanning speed 200 mm/s

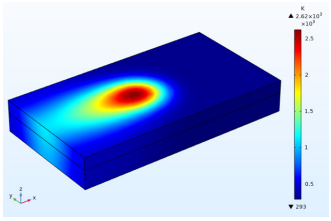

(c) Laser power 100 W, Scanning speed 300 mm/s

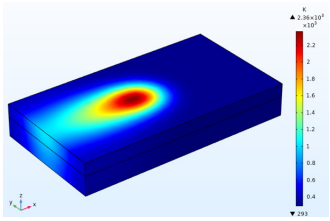

(d) Laser power 100 W, Scanning speed 400 mm/s

Fig. 2 Temperature distribution of single track simulation

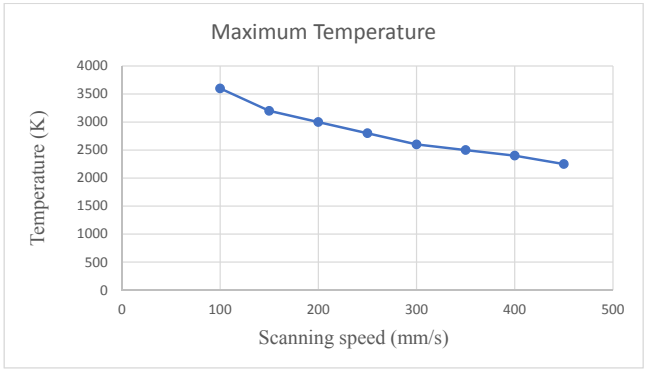

Fig. 3 Maximum temperature varies with scanning speed

3.1.3 Isothermal contour

From Figure 4, with the rising speed, the shape of the isothermal contour gradually turned to bullet like shape. The width of the isothermal contour decreased as the scanning speed increased. The length of the isothermal contour increased as the scanning speed increased. The front isothermal contour gradually tilts with the growing scanning speed, which means that the heat conducting speed has been gradually caught up by scanning speed.

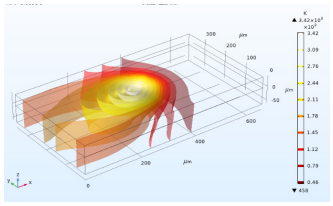

(a) Laser power 100 W, Scanning speed 100 mm/s

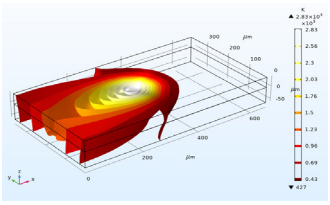

(b) Laser power 100 W, Scanning speed 200 mm/s

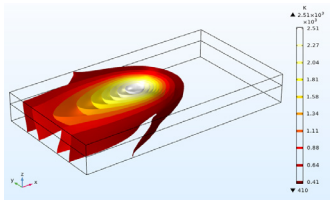

(c) Laser power 100 W, Scanning speed 300 mm/s

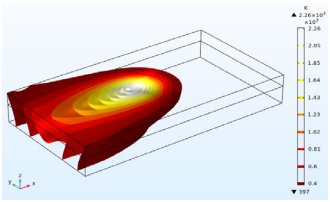

(d) Laser power 100 W, Scanning speed 400 mm/s

Fig. 4 Isothermal contour of single track simulation

3.1.4 Single track simulation versus experiment

Figure 5 shows the single track simulation and experiment results. The track width from simulation is consistent with the track width from the experiment. The width of single track reduced while the scanning speed increased as shown in Figure 5. The widest single trajectory appears in the model of scanning speed 100 mm/s which of the VED is 416 J/mm3. The VED decreases with the increasing scanning speed, as shown in Figure 6. As Figure 7 shows, with the growing VED, the track width elevates from 100 μm to 255 μm, in other word, as the scanning speed increases, the track width decreases.

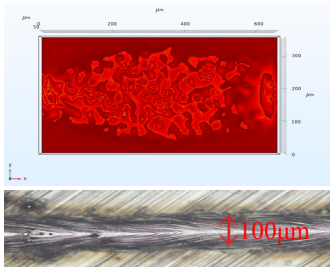

(a) Track width 255μm (Laser power 100 W, Scanning speed 100 mm/s)

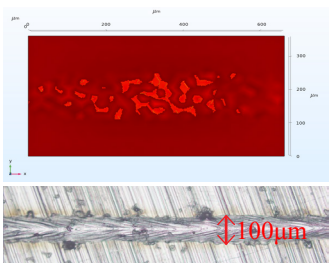

(b) Track width 145μm (Laser power 100 W, Scanning speed 200 mm/s)

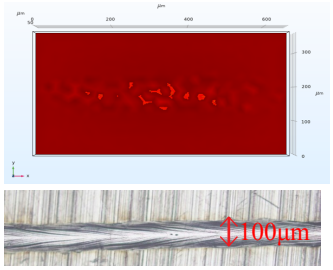

(c) Track width 110μm (Laser power 100 W, Scanning speed 300 mm/s)

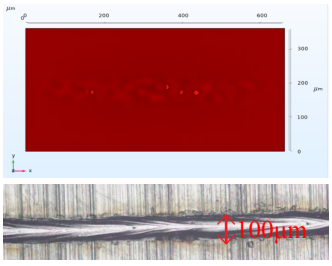

(d) Track width 95μm (Laser power 100 W, Scanning speed 400 mm/s)

Fig. 5 Track width of single molten track varies with scanning speed

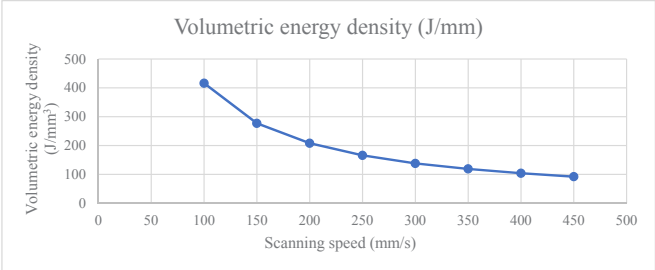

Fig. 6 Volumetric energy density varies with scanning speed

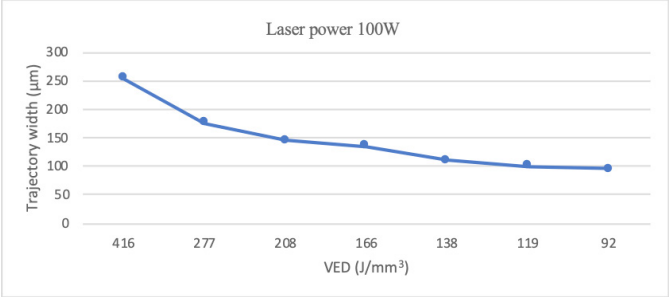

Fig. 7 Width of single track simulation

3.1.5 Effect of scanning speed with enthalpy on manufacturing parts

Figure 8 shows the enthalpy in single track model, as the scanning speed increases, the enthalpy decreases, which means that the energy inside the manufacturing parts is decreasing due to the increasing scanning speed. The tendency of the enthalpy in single track model fits the tendency of the track width, VED, and maximum temperature in the experiment data.

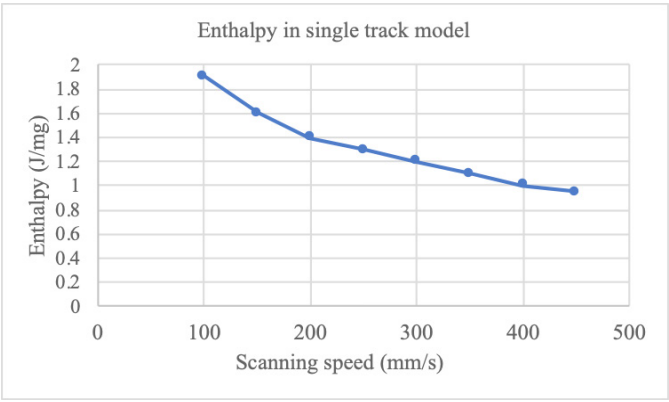

Fig. 8 Enthalpy in single track model

3.2 Analysis and Validation of Single Layer Simulation

In order to find the relations between the single layer and the temperature distribution, the width of single molten track must be found first. Figure 9 Shows the width of the single track obtained by simulation.

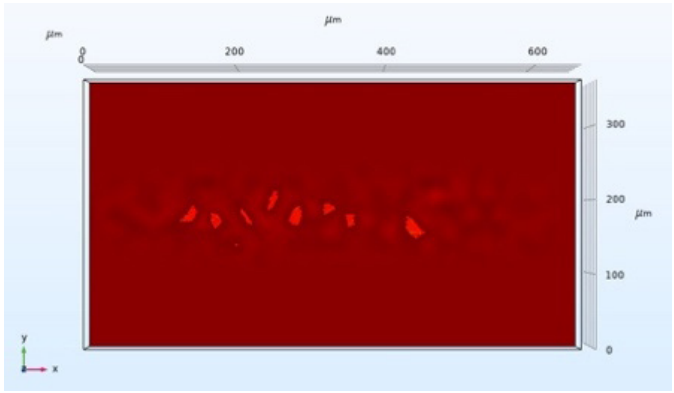

(a) Track width 120μm

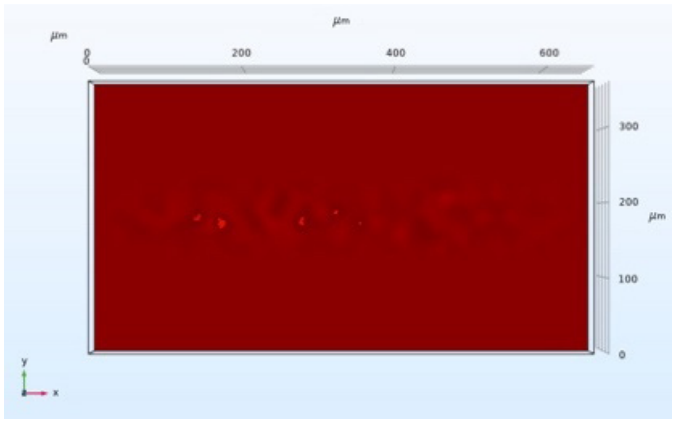

(b) Track width 85μm

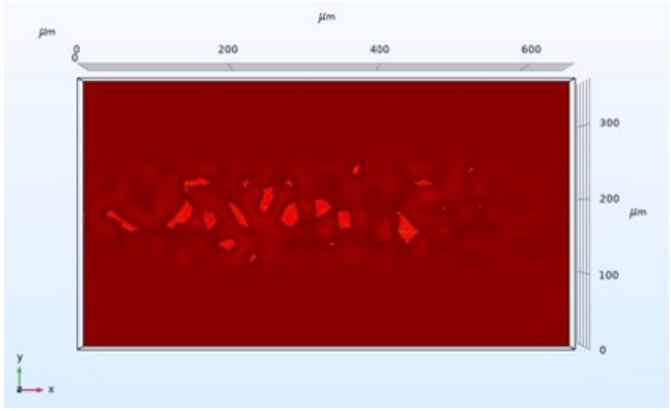

(c) Track width 130μm

Fig. 9 Width of the single track under (a) laser power 150W, scanning speed 500 mm/s; (b) laser power 150 W, scanning speed 650 mm/s; (c) laser power 200 W, scanning speed 500 mm/s.

In the single layer simulation, the overlap ratio is determined to be 30%, the scan line spacing can be determined when the track width been found. The scan line spacing and VED of three parameters are listed in Table 3.

Table 3 The scan line spacing and VED.

Laser power	Scanning speed(mm/s)	Track width(μm)	Scan line spacing (μm)	VED (J/mm3)
150 W	500	120.0	84.0	137.93
150 W	650	85.0	59.5	106.10
200 W	500	130.0	91.0	183.91

3.2.1 Temperature distribution varies with Time

Figure 10 shows the simulation result of the single layer, with increasing molten tracks, the temperature gradually increased to 3.73×103K, which is at the 0.012 s of scanning time, the total scanning time is 0.022 s. The reason that the temperature stops raising is that the rate of energy obtained from the laser and the rate of energy lost from conduction, convection and radiation achieve to a balance state.

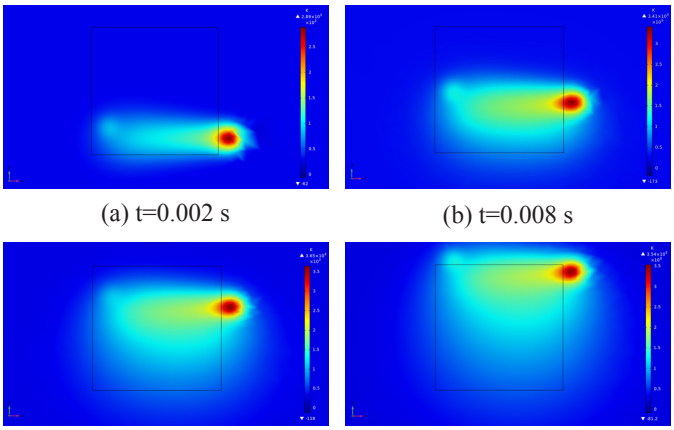

(a) t=0.002 s (b) t=0.008 s

(c) t=0.014 s (d) t=0.0020 s

Fig. 10 Temperature distribution of the single layer under laser power 200W, scanning speed 500 mm/s, overlap ratio 30%

3.2.2 Maximum temperature of the single layer simulation

The maximum temperature varies with time and the simulation results are plot in Figure 11, Figure 12, Figure 13. The maximum temperature rises rapidly when the laser starts to heat the powder layer, and reaches to the temperature around 3200 K, 3100K, 4200K, respectively. The maximum temperature of crests raises gradually till the equilibrium of the energy balance. The valley in the plot appears when the laser stops to heat the powder layer and starts to heat the next scanning track. The SLM specimen under three sets of process parameters and the roughness measured results are showed in Figure 14. Comparing the simulation and experiment results, it was found that that the maximum temperature around vaporing temperature of the material has the better surface roughness. The worst surface quality go with the distortion of specimen appears when the maximum temperature exceeds much more than the vaporing temperature. The last crest in the Figure 11 and 13 are lower than previous crests which is because the laser beam in the last path is part out of the observing region, and only parts of energy have been obtained.

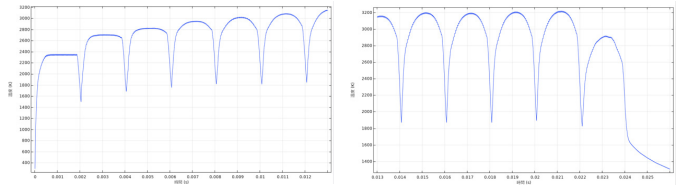

(a) t=0 s ~ t=0.012998 s (b) t=0.012998 s～ t=0.025998 s

Fig. 11 Maximum temperature under laser power 150W, scanning speed 500 mm/s, overlap ratio 30%, (a) t=0 s ~ t=0.012998 s, (b) t=0.012998 s ~ t=0.025998 s.

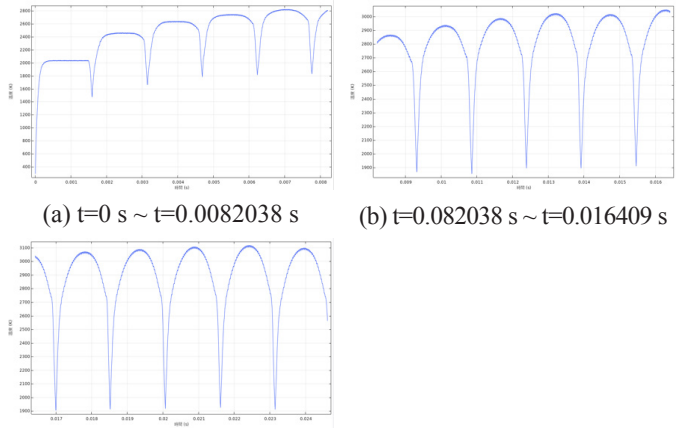

(a) t=0 s ~ t=0.0082038 s (b) t=0.082038 s ~ t=0.016409 s

(c) t=0.016409 s ~ t=0.024615 s

Fig. 12 Maximum temperature under laser power 150W, scanning speed 650 mm/s, overlap ratio 30%, (a) t=0 s ~ t=0.0082038 s, (b) t=0.082038 s ~ t=0.016409 s, (c) t=0.016409 s ~ t=0.024615 s

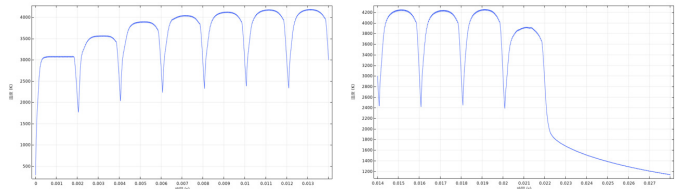

(a) t=0 s ~ t=0.012998 s (b) t=0.012998 s ~ t=0.025998 s

Fig. 13 Maximum temperature under laser power 200W, scanning speed500 mm/s, overlap ratio 30%, (a) t=0 s ~ t=0.012998 s, (b) t=0.012998 s ~ t=0.025998 s.

(a) Ra 11.7 (b) Ra 10.6 (c) Surface distortion

Fig. 14 SLM specimen under different process parameters: (a) laser power 150W, scanning speed 500 mm/s, overlap ratio 30%, (b) laser power 150W, scanning speed 650 mm/s, overlap ratio 30%, (c) laser power 200W, scanning speed 500 mm/s, overlap ratio 30%.

4. DISCUSSION

The investigation of temperature distribution on the surface roughness of the SLM specimen was presented in this study. The simulation results were compared with the experimental results of SLM process. In the single melting track simulation, the results of track width were consistent with track widths on SLM specimen. In the multiple track simulation, the relationship between temperature distribution and surface roughness of specimen was investigated. The main conclusions in this research are summarized as follows:

1. In this study, a finite-element simulation of heat transfer was applied for the validation of temperature distribution in the single powder layer. The FEM simulation is utilized to analyze the relationship in the process parameters, volumetric energy density, temperature distribution, track width and surface roughness.
2. The width of single track decreased with the decreasing of volumetric energy density. With the same laser power, the track width is narrower as the faster scanning speed. The temperature is proportional with the VED magnitude, the higher the VED, the lower the temperature. The iso-contour of temperature formed to bullet like as VED decreased.
3. The enthalpy deceases with the decreasing scanning speed, which fits the tendency of the single track width that the lower VED values, the narrower track width.
4. In multiple track simulation, the temperature increases as the number of scan track increases until the maximum temperature, and the thermal accumulation effect is clearly observed in the temperature profile.
5. The simulation and experiment result shows that the maximum temperature around vaporing temperature of the material has the better surface roughness. The worst surface roughness of specimen appears when the maximum temperature exceeds much more than the vaporing temperature.
6. According to the multiple track simulation results, the first track of the model does not reach the temperature around vaporing point, which might not achieve to the best surface quality. It is necessary to pre-heat the particle layer before manufacturing.

ACKNOWLEDGEMENT

The authors gratefully acknowledge Ministry of Science and Technology for the financial support to this study (grant numbers 107-2221-E-224-057 and 108-2221-E-224-047-MY2).

REFERENCES

Baumers, M.; Dickens, P.; Tuck, C.; Hague, R. The cost of additive manufacturing: machine productivity, economies of scale and technology-push. Technol. *Forecast. Soc. Change* 2016, **102**, 193-201.

Ngo, T. D.; Kashani, A.; Imbalzano, G.; Nguyen, K. T.; Hui, D. Additive manufacturing (3D printing): A review of materials, methods, applications and challenges. *Compos. B. Eng*. 2018, **143**, 172-196.

The global additive manufacturing market 2018 is worth $9.3 billion. Available online: https://www.3dprintingmedia.network/the-global-additive-manufacturing-market-2018-is-worth-9-3-billion/ (accessed on Feb 16, 2019)

Yap, C. Y.; Chua, C. K.; Dong, Z. L.; Liu, Z. H.; Zhang, D. Q.; Loh, L. E.; Sing, S. L. Review of selective laser melting: Materials and applications. *Appl. Phys. Rev*. 2015, **2**(4), 041101.

Zhang, B.; Li, Y.; Bai, Q. Defect formation mechanisms in selective laser melting: a review. *Chin. J. Mech. Eng*. 2017, **30**(3), 515-527.

Zeng, K.; Pal, D.; Stucker, B. A review of thermal analysis methods in laser sintering and selective laser melting. Proceedings of Solid Freeform Fabrication Symposium, Austin, TX, August ,2012. (Vol. 60, pp. 796-814).

Wu, J.; Wang, L.; An, X. Numerical analysis of residual stress evolution of AlSi10Mg manufactured by selective laser melting. *Optik* 2017, **137**, 65-78.

Yadroitsev, I.; Smurov, I. Surface morphology in selective laser melting of metal powders. *Phys. Procedia* 2011, **12**, 264-270.

Cherry, J. A.; Davies, H. M.; Mehmood, S.; Lavery, N. P.; Brown, S. G. R.; Sienz, J. Investigation into the effect of process parameters on microstructural and physical properties of 316L stainless steel parts by selective laser melting. *Int. J. Adv. Manuf. Technol*. 2015, **76**(5-8), 869-879.

Bourell, D.; Stucker, B.; Spierings, A. B.; Herres, N.; Levy, G. Influence of the particle size distribution on surface quality and mechanical properties in AM steel parts. *Rapid Prototyp*. J. 2011, **17**(3), 195-202.

Mumtaz, K.; Hopkinson, N. Top surface and side roughness of Inconel 625 parts processed using selective laser melting. *Rapid Prototyp*. J. 2009, **15**(2), 96-103.

Rombouts, M.; Froyen, L.; Gusarov, A. V.; Bentefour, E. H.; Glorieux, C. Light extinction in metallic powder beds: Correlation with powder structure. *J. Appl. Phys*. 2005, **98**(1), 013533.

Wang, L.; Wei, Q. S.; Shi, Y. S.; Liu, J. H.; He, W. T. Experimental investigation into the single-track of selective laser melting of IN625. *Adv. Mat. Res*. 2011, **233**, 2844-2848.

Hong, M. H.; Min, B. K.; Kwon, T. Y. The influence of process parameters on the surface roughness of a 3D-printed Co–Cr dental alloy produced via selective laser melting. *Appl. Sci*. 2016, **6**(12), 401.

Ciurana, J.; Hernandez, L.; Delgado, J. Energy density analysis on single tracks formed by selective laser melting with CoCrMo powder material. *Int. J. Adv. Manuf. Technol*. 2013, **68**(5-8), 1103-1110.

Gong, H.; Rafi, K.; Gu, H.; Ram, G. J.; Starr, T.; Stucker, B. Influence of defects on mechanical properties of Ti–6Al–4 V components produced by selective laser melting and electron beam melting. *Mater. Des*. 2015, **86**, 545-554.

Di, W.; Yongqiang, Y.; Xubin, S.; Yonghua, C. Study on energy input and its influences on single-track, multi-track, and multi-layer in SLM. *Int. J. Adv. Manuf. Technol*. 2012, **58**(9-12), 1189-1199.

Hussein, A.; Hao, L.; Yan, C.; Everson, R. Finite element simulation of the temperature and stress fields in single layers built without-support in selective laser melting. *Mater. Des*. 2013, **52**, 638-647.

Li, Y.; Gu, D. Parametric analysis of thermal behavior during selective laser melting additive manufacturing of aluminum alloy powder.

Mater. Des. 2014, 63, 856-867.

Loh, L. E.; Chua, C. K.; Yeong, W. Y.; Song, J.; Mapar, M.; Sing, S. L.; Liu, Z. H.; Zhang, D. Q. Numerical investigation and an effective modelling on the Selective Laser Melting (SLM) process with aluminium alloy 6061. *Int. J. Heat Mass Transf*. 2015, **80**, 288-300.

Alkahari, M. R.; Furumoto, T.; Ueda, T.; Hosokawa, A.; Tanaka, R.; Abdul Aziz, M. S. Thermal conductivity of metal powder and consolidated material fabricated via selective laser melting. *Key Eng. Mater*. 2012, **523**, 244-249.

Antony, K.; Arivazhagan, N.; Senthilkumaran, K. Numerical and experimental investigations on laser melting of stainless steel 316L metal powders. *J. Manuf. Process* 2014, **16**(3), 345-355.

Foroozmehr, A.; Badrossamay, M.; Foroozmehr, E.; Golabi, S. I. Finite element simulation of selective laser melting process considering optical penetration depth of laser in powder bed. *Mater. Des*. 2016, **89**, 255-263.

Yin, J.; Zhu, H.; Ke, L.; Lei, W.; Dai, C.; Zuo, D. Simulation of temperature distribution in single metallic powder layer for laser micro-sintering. *Comput. Mater. Sci*. 2012, **53**(1), 333-339.

Dong, L.; Makradi, A.; Ahzi, S.; Remond, Y. Three-dimensional transient finite element analysis of the selective laser sintering process. *J. Mater. Process. Technol*. 2009, **209**(2), 700-706.

Trapp, J.; Rubenchik, A. M.; Guss, G.; Matthews, M. J. In situ absorptivity measurements of metallic powders during laser powder-bed fusion additive manufacturing. *Appl. Mater. Today* 2017, **9**, 341-349.

Rombouts, M.; Kruth, J. P.; Froyen, L.; Mercelis, P. Fundamentals of selective laser melting of alloyed steel powders. *CIRP annals* 2006, **55**(1), 187-192.

Sih, S. S.; Barlow, J. W. The prediction of the thermal conductivity of powders. In International Solid Freeform Fabrication Symposium, 1995.

COMSOL. CFD Module users guide, 5.4; 2018; pp 128-129.

COMSOL. CFD Module users guide, 5.4; 2018; pp 400-402.